Inherent Spin-Orbit Locking in Topological Lasing via Bound State in the Continuum

Jiajun Wang,[1,*] Xinhao Wang,[1] Zhaochen Wu,[1] Xingqi Zhao,[1] Shunben Wu,[1] Lei Shi,[1,3,4,5,†] Yuri Kivshar,[2,‡] and Jian Zi[1,3,4,5,§]

[1]State Key Laboratory of Surface Physics, Key Laboratory of Micro- and Nano-Photonic Structures (Ministry of Education) and Department of Physics, Fudan University, Shanghai 200433, China
[2]Nonlinear Physics Centre, Research School of Physics, The Australian National University, Canberra ACT 2601, Australia
[3]Institute for Nanoelectronic Devices and Quantum Computing, Fudan University, Shanghai 200438, China
[4]Collaborative Innovation Center of Advanced Microstructures, Nanjing University, Nanjing 210093, China
[5]Shanghai Research Center for Quantum Sciences, Shanghai 201315, China

(Received 23 September 2024; accepted 3 March 2025; published 4 April 2025)

Bound states in the continuum (BICs) are exotic optical topological singularities that defy the typical radiation within the continuum of radiative modes and carry topological polarization vortices in momentum space. Enabling ultrahigh quality factors, BICs have been applied in realizing lasing and Bose-Einstein condensation, and their momentum-space vortex topologies have been exploited in passive systems, revealing novel spin-orbit photonic effects. Here, we demonstrate the inherent spin-orbit locking in topological BIC lasing. Utilizing C_{4v} and C_{6v} photonic crystal slabs, we achieve distinct spin-orbit locking combinations in BIC lasing of $+1$ and -2 topological charges. Spin-orbit locking phenomena are directly observed by momentum-space spin-dependent self-interference patterns. Real-space spin separations, as a counterpart of the momentum-space spin-orbit locking, are also revealed. Our results reveal new spin-orbit locking phenomena in BIC lasing, presenting significant potential for advancements in topological photonic source applications.

DOI: 10.1103/PhysRevLett.134.133802

Bound states in the continuum (BICs), initially proposed in quantum mechanics, have since established themselves as pivotal phenomena in modern photonics due to their rich physical implications [1–4]. With infinite quality factors, BICs stand as topological optical singularities that remain perfectly confined within the continuum of radiative modes [5,6]. Especially in periodic structures like photonic crystal (PhC) slabs, BICs are found to carry complex topological polarization vortices in momentum space [7–9]. These properties of BICs have been utilized to enhance versatile applications in various areas such as sensors [10,11], lasers [12–16], Bose-Einstein condensation [17,18], light-matter interaction [19–21], and spin-orbit interaction of light [22,23]. In particular, the momentum-space vectorial topology of BICs, out of the well-known topological band theory for scalar fields, gives rise to new perspectives of topological photonics in the far field.

For optical fields in free space, the spin angular momentum and orbital angular momentum (OAM) of light are two crucial indices of light, being related to circular polarizations ($\sigma_{\pm}$) and the winding number (l) of the spiral phase [24–26]. Exploring the relation and interaction between the spin angular momentum and OAM of light has attracted great attention in photonics. In vectorial optical fields, spin and orbit are inherently connected, underlying unique phenomena in spin-orbit photonics [27–30]. From this perspective, novel topological spin-orbit phenomena are anticipated in momentum-space vectorial polarization vortex configurations of BICs. On the one hand, spin-orbit interactions of light have been explored in resonance-induced modulations for incident light. The incident-polarization-dependent effects like spin-to-vortex conversion and the photonic spin Hall effect are proposed and demonstrated via polarization vortices around BICs [22,23]. On the other hand, radiations based on BICs will inherit properties of BICs, and polarization vortices are observed in BIC-modulated emission such as lasing and Bose-Einstein condensation [12–18]. Further explorations of spin-orbit properties in BIC lasing hold great importance for basic research and practical applications. However, to date, lasing phenomena of BICs with spin-orbit properties have not been explored.

In this work, we demonstrate the inherent spin-orbit locking in topological BIC lasing. Spin-orbit locking lasing behaviors are inherent from topological polarization configurations of BICs. By taking advantage of various momentum-space topological configurations of BICs, we can realize different spin-orbit locking combinations in BIC

*Contact author: jiajunwang@fudan.edu.cn
†Contact author: lshi@fudan.edu.cn
‡Contact author: yuri.kivshar@anu.edu.au
§Contact author: jzi@fudan.edu.cn

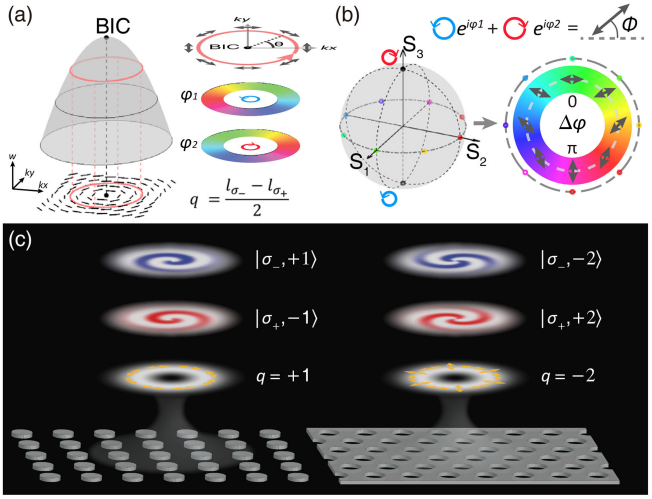

FIG. 1. (a) Schematic of a photonic band and momentum-space polarization vortex. Vortex polarization configuration underlies inherent spin-orbit locking of BICs, corresponding to spin-dependent phase winding numbers $l_{\sigma_\pm}$. (b) Poincaré sphere representation for spin-dependent phase vortices. (c) Schematic view of the proposed spin-orbit locking $|\sigma_\pm, l\rangle$ in topological BIC lasing.

lasing. C_{4v} and C_{6v} PhC slabs were applied to demonstrate various spin-orbit locking properties in BIC lasing. Both vortex and high-order antivortex polarization configurations were realized in BIC microlasers with $+1$ and -2 topological charges. By momentum-space spin-dependent self-interference patterns of lasing profiles, the inherent spin-orbit locking in BIC lasing was directly identified. Corresponding real-space spin separations were also observed.

Figure 1(a) schematically depicts a photonic band with a BIC. This BIC carries $+1$ topological charge, embodying the momentum-space polarization vortex. The spin-orbit related properties are inherent in the topological configuration of BICs. For example, surrounding this BIC along the magenta circle, the orientation of the polarization state rotates anticlockwise as the azimuth angle θ increases. The $+1$ topological charge of the BIC corresponds to a total accumulated winding angle of $+2\pi$. When considering two spin components of these polarization states ($\sigma_\pm$), we can see that opposite spiral phase windings exist along the magenta circle in momentum space. In other words, the phase distributions of two spin components form phase vortices with opposite phase winding numbers (orbit, l). Each spin is locked with a specific OAM l. In the case shown in Fig. 1(a), the left-handed circular polarization (σ_-) carries a positive phase optical vortex ($l = 1$), and the right-handed circular polarization (σ_+) carries a negative phase optical vortex ($l = -1$).

The origin of this spin-orbit locking can be understood using the Poincaré sphere representation, as shown in Fig. 1(b). We consider linear polarization state $|E(\phi)\rangle$ for an example, which can be decomposed by two poles ($|\sigma_\pm\rangle$) of the Poincaré sphere as

$$|E(\phi)\rangle = e^{i\varphi_1}|\sigma_-\rangle + e^{i\varphi_2}|\sigma_+\rangle,$$
$$\phi = \frac{\varphi_1 - \varphi_2}{2} = \frac{\Delta\varphi}{2}. \tag{1}$$

Here, ϕ is defined as the polarization orientation angle of the linear polarization state, and φ_1, φ_2 are phases of the spin basis. The polarization orientation angle ϕ is equal to half of the phase difference $\Delta\varphi$ of two spin components. As exhibited in the right panel of Fig. 1(b), winding along the equator of the Poincaré sphere, $\Delta\phi$ varies continuously with ϕ. We can project polarization vortices carried by BICs onto the Poincaré sphere, and then the topological charge q of the BIC can be written as

$$q = \frac{1}{2\pi}\oint_C \frac{\partial\phi}{\partial\theta}\mathrm{d}\theta = \frac{1}{4\pi}\oint_C \left(\frac{\partial\varphi_1}{\partial\theta} - \frac{\partial\varphi_2}{\partial\theta}\right)\mathrm{d}\theta = \frac{l_{\sigma_-} - l_{\sigma_+}}{2}. \tag{2}$$

Here, C is a loop around the BIC in momentum space, such as the magenta circle in Fig. 1(a), and $l_{\sigma_\pm}$ is the accumulated phase winding number of the $\sigma_\pm$ component. We can see that the spin-orbit locking $|\sigma_\pm, l\rangle$ properties are inherent in topological charges of BICs. For the mostly discussed symmetry-protected BICs, we consider the existence of one mirror symmetry; then l_{σ_-} is equal to $-l_{\sigma_+}$. We can simplify Eq. (2) as

$$q = l_{\sigma_-} = -l_{\sigma_+}. \tag{3}$$

From this perspective, various spin-orbit locking $|\sigma_\pm, l\rangle$ exist in BICs with different topological charges. The allowed topological charge of BICs are constrained by the symmetries of PhC slabs. For the relations between symmetries and topological charges, see Supplemental Material [31].

As the significant application of BICs, BIC lasing has inherent spin-orbit locking properties. Figure 1(c) exhibits schematics of two examples of BIC lasing with distinct spin-orbit locking behaviors. The first one utilizes the BIC of $+1$ topological charge in a C_{4v} PhC slab. The total lasing profile is a vortex-polarization-configuration vectorial beam, and inherent spin-orbit locking relations are $|\sigma_\pm, \mp 1\rangle$. This means that the σ_- lasing component is a vortex beam with $+2\pi$ spiral phase winding and the σ_+ lasing component is a vortex beam with -2π spiral phase winding. The second one utilizes the BIC of -2 topological charge in a C_{6v} PhC slab. The total lasing profile is an antivortex-polarization-configuration vectorial beam, and inherent spin-orbit locking relations are $|\sigma_\pm, \pm 2\rangle$.

To demonstrate spin-orbit locking phenomena in BIC lasing, we designed two types of PhC slabs with different symmetries (C_{4v} and C_{6v}). PhC structures are composed of silicon nitride (Si_3N_4, refractive index ~ 2) in an

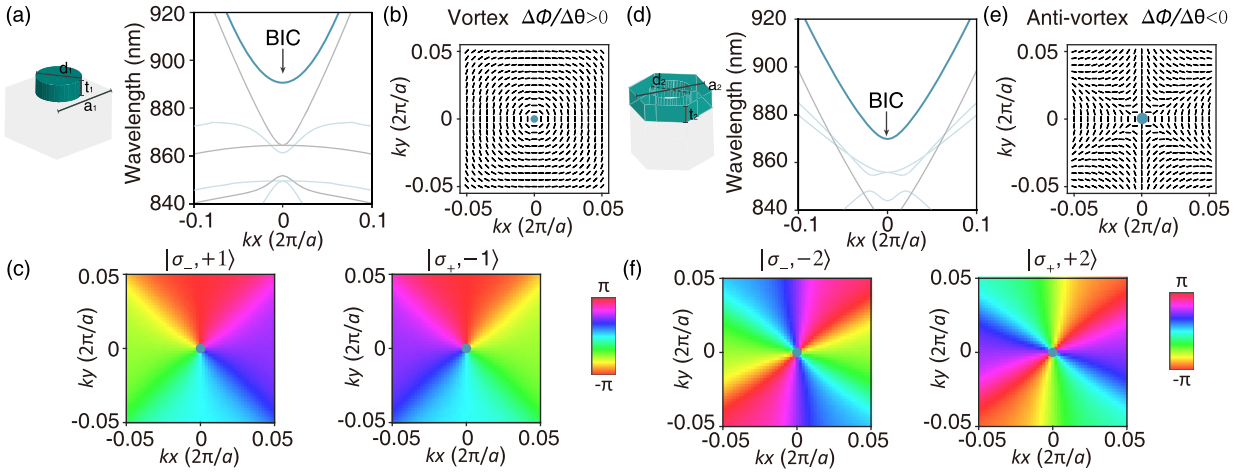

FIG. 2. (a) Unit cell of the designed C_{4v} PhC slab and the simulated photonic bands. (b) Momentum-space polarization vortex on the cyan-colored photonic band in (a), in which the topological charge of the BIC is $+1$. (c) Spin-dependent phase distributions in momentum space for the $+1$ BIC. (d) Unit cell of the designed C_{6v} PhC slab and the simulated photonic bands. (e) Momentum-space polarization vortex on the cyan-colored photonic band in (d), in which the topological charge of the BIC is -2. (f) Spin-dependent phase distributions in momentum space for the -2 BIC.

environment of optical silica (refractive index ∼1.45). Figure 2(a) shows the schematic of the C_{4v} PhC slab. The unit cell consists of a circular Si_3N_4 pillar with lattice constant a_1 of 560 nm, pillar diameter d_1 of 420 nm, and slab thickness t_1 of 240 nm. The corresponding photonic band structure, depicted in the right panel of Fig. 2(a), demonstrates a symmetry-protected BIC at the Γ point with a $+1$ topological charge. Figure 2(b) shows the momentum-space polarization distribution around the BIC. Then, by decomposing eigen polarization distributions using circular polarization bases based on Eq. (1), we calculated momentum-space phase distributions of two spin components, as shown in Fig. 2(c). The results show that the σ_- component carries a positive phase vortex ($l = +1$) and the σ_+ component carries a negative phase vortex ($l = -1$), agreeing well with Eq. (3). Similarly, Fig. 2(d) illustrates the schematic of the C_{6v} PhC slab, composed of a triangular array of etched circular holes in a Si_3N_4 film. The lattice constant a_2 is 634 nm, hole diameter d_2 is 320 nm, and slab thickness t_2 is 120 nm. The right panel of Fig. 2(d) shows the corresponding photonic band structure, in which the arrow marks the required symmetry-protected BIC at the Γ point with a -2 topological charge. Figure 2(e) shows the antivortex polarization configuration around the BIC. The calculated momentum-space phase distributions in Fig. 2(f) show that the σ_- component carries a positive phase vortex ($l = -2$) and the σ_+ component carries a negative phase vortex ($l = +2$).

To experimentally implement the proposed spin-orbit locking in BIC lasing, we then fabricated the designed two types of PhC slabs. Figures 3(a) and 3(d) show the scanning electron microscopy images and corresponding measured momentum-resolved transmittance spectra of fabricated C_{4v} and C_{6v} samples, respectively. Black arrows mark the designed two types of BICs in Fig. 2.

To realize BIC lasing, we chose IR-140 dye molecules as the gain and dissolved them in dimethyl sulfoxide to match the refractive index of the optical silica. The experimental setup is shown in Supplemental Material [31]. Figures 3(b) and 3(e) exhibit the measured above-threshold integrated lasing spectra and input-output integrated photoluminescence curves (insets) corresponding to samples shown in Figs. 3(a) and 3(b). Obvious lasing features were observed including characteristic threshold behaviors and sharp peaks. Figures 3(c) and 3(f) show momentum-space BIC lasing profiles of $+1$ and -2 topological charges. Momentum-space topological polarization configurations of the BIC lasing were examined by taking polarization-resolved images. For the lasing profile via BIC of $+1$ topological charge, there are two nodes for certain linear polarization; as the polarization direction rotates anticlockwise, the nodes rotate along the same direction. For the lasing profile via BIC of -2 topological charge, there are four nodes for certain linear polarization; as the polarization direction rotates anticlockwise, the nodes rotate along the opposite direction.

To directly observe the spin-orbit locking in BIC lasing, we performed self-interference experiments [32,38], shown in Fig. 4. In self-interference patterns of the $\sigma_\mp$ components, fork-shaped interference fringes were observed. Dashed lines marked the fringe splitting. For lasing profiles via BIC of $+1$ topological charge [Fig. 4(a)], one fringe is split into two in the centers of the lasing profiles, indicating that the absolute OAM $|l|$ is equal to 1. When changing from σ_- to σ_+, we can see that the direction of the fork-shaped fringes reverses, corresponding to reversed signs of the OAM l. The σ_- lasing profile carries an OAM of $+1$, and the σ_+ lasing profile carries an OAM of -1. For details about the sign of the OAM l, see Supplemental Material [31].

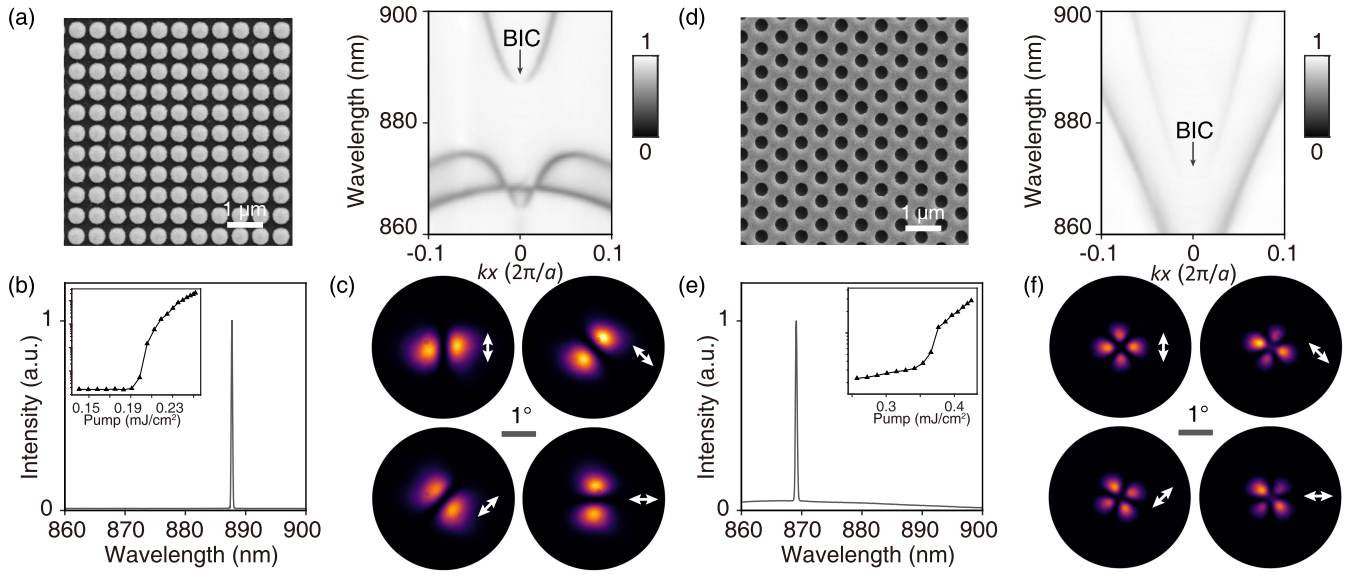

FIG. 3. (a),(d) Scanning electron microscopy images of the fabricated PhC slabs and corresponding measured momentum-resolved transmittance spectra. (a) C_{4v} PhC slab. (d) C_{6v} PhC slab. (b),(e) Measured above-threshold integrated lasing spectra and momentum-resolved lasing spectra via PhC slabs of (a) and (d). Insets shows input-output integrated photoluminescence curves. a.u., arbitrary units. (c),(f) Measured polarization-resolved lasing images in momentum space via PhC slabs of (a) and (d). Double arrows show directions of analyzed polarizations.

For lasing profiles via the BIC of −2 topological charge [Fig. 4(b)], one fringe is split into three in the centers of the lasing profiles, indicating that the absolute OAM $|l|$ is equal to 2. The spin-orbit locking was also observed where the σ_- lasing profile carries an OAM of −2 and the σ_+ lasing profile carries an OAM of +2. Notably, for the same spin components (σ_- or σ_+) of lasing profiles via BICs of +1 and −2 topological charges, the directions of fork-shaped fringes are opposite to each other, demonstrating different spin-orbit locking behaviors governed by topological charges of BICs [Eq. (3)]. Furthermore, we analyze the purity of these lasing profiles to exhibit a relatively high OAM purity (Supplemental Material [31]).

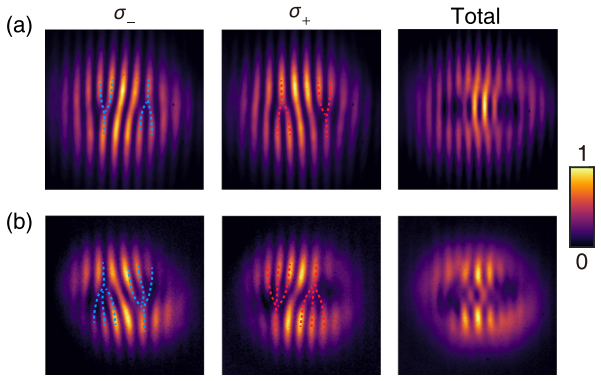

FIG. 4. (a) Measured self-interference patterns of the BIC lasing profiles of +1 topological charge. (b) Measured self-interference patterns of the BIC lasing profiles of −2 topological charge.

In contrast, for self-interference patterns of total lasing profiles, there are not such obvious fork-shaped interference patterns, meaning the absence of spiral phases. Based on previous discussions in theoretical parts, we can know that two spin-orbit coupled components in conventional BICs are degenerate; hence the total OAM is zero. From this perspective, we also experimentally demonstrated the zero total OAM in conventional BIC lasing. This inspires the future development of BIC lasing with nonzero OAM by introducing additional symmetry breaking to change the distribution of two spin components or lift the spin degeneracy [39,40].

Moreover, besides spin-related self-interference patterns in momentum space, the spin-orbit locking can also manifest as spin separations in real space. In discussions of spin-orbit locking based on topological polarization configurations, we have known that two spin components carry opposite OAM in momentum space, i.e., opposite tangential phase gradients. Such spin-dependent momentum-space phase gradients correspond to spin-dependent separations of real-space position $\langle \boldsymbol{R}_{\sigma_\pm} \rangle$ [23,29,41] as

$$\langle \boldsymbol{R}_{\sigma_\pm} \rangle = -\left\langle \frac{\partial \varphi_{\sigma_\pm}(\boldsymbol{k}_{||})}{\partial \boldsymbol{k}_{||}} \right\rangle. \tag{4}$$

Here, $\langle \boldsymbol{R}_{\sigma_\pm} \rangle$ is the lasing profile in real space, $\boldsymbol{k}_{||}$ is the projected in-plane momentum, and $\varphi_{\sigma_\pm}(\boldsymbol{k}_{||})$ is the phase of the $\sigma_\pm$-component lasing profile at certain $\boldsymbol{k}_{||}$. To observe expected spin separations, an iris was put on the Fourier plane relative to the sample, and only one part

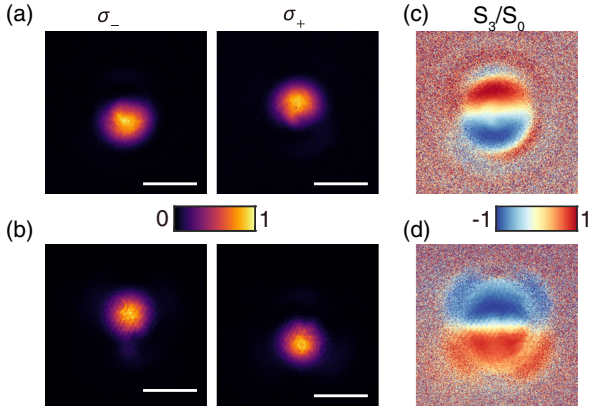

FIG. 5. (a),(b) Experimental observation of spin separations in real space for the filtered lasing profiles. (a) +1 BIC lasing. (b) −2 BIC lasing. Scale bars: 100 μm. (c),(d) Normalized third Stokes parameters in real space calculated from (a) and (b).

of doughnut-shaped lasing profiles was filtered to pass through. The spin-dependent lasing profiles $I_{\sigma_\pm}$ were captured by a camera put on the real-image plane of the sample, as shown in Figs. 5(a) and 5(b). To clearly exhibit the spin separations, we further calculated the distribution of the normalized third Stokes parameter by $(S_3/S_0) = ([I_{\sigma_+} - I_{\sigma_-}]/[I_{\sigma_+} + I_{\sigma_-}])$, as shown in Figs. 5(c) and 5(d). Clear spin separations were observed. There are opposite spin separations for BIC lasing of +1 topological charge [Figs. 5(a) and 5(c)] and −2 topological charge [Figs. 5(b) and 5(d)]. The BIC lasing has spin-dependent near-field distributions of emission profiles and manifests as spin-orbit locking in far field.

The unique spin-orbit locking properties in BIC lasing are important for both BICs and lasing research areas. In previous lasing studies via BICs, high Q factors are first explored to realize lasing [12,13,42,43], and then topological polarization configurations of BICs are applied to realize vectorial polarization vortex lasing [14–16,44,45]. Here, beyond topological polarization configurations, inherent spin-orbit locking in BICs is further discovered and utilized to realize various spin-orbit locking lasing. The spin-orbit locking lasing, due to the potential in light-field manipulation and information processing, has attracted much research attention in the last decade [26,46] and has been realized in various systems [32,33,38,47–50]. BICs offer a new nonlocal method to develop compact spin-orbit locking microlasers, and topological charges of BICs offer a new degree of freedom to manipulate both the spin-orbit relations and OAM orders.

In this work, we have explored the inherent spin-orbit locking in topological BIC lasing using PhC slabs with different symmetries. Our findings demonstrate that spin-orbit locking behavior of BICs can be harnessed to achieve switchable OAM lasing by controlling spins. Experimental results confirmed momentum-space spin-dependent phase vortices and revealed real-space spin separations in BIC lasing, directly tied to topological configurations of BICs. These results not only deepen our understanding of the interplay between spin and orbital angular momentum in photonic systems but also pave the way for novel applications in spin-controlled photonic devices and topological photonics.

Acknowledgments—We thank Dr. T. Y. Li for helpful discussions. This work was supported by the National Key R&D Program of China (Grants No. 2023YFA1406900 and No. 2022YFA1404800); National Natural Science Foundation of China (Grants No. 12234007, No. 12321161645, No. 12221004, No. T2394480, No. T2394481, and No. 12404427); and Science and Technology Commission of Shanghai Municipality (Grants No. 22142200400, No. 21DZ1101500, No. 2019SHZDZX01, No. 23DZ2260100, and No. 24YF2702400). J. W. was further supported by the China National Postdoctoral Program for Innovative Talents (Grant No. BX20230079) and the China Postdoctoral Science Foundation (Grant No. 2023M740721).

J. W. and X. W. contributed equally to this Letter.

Data availability—The data supporting this study's findings are available within the Letter.

[1] C. W. Hsu, B. Zhen, A. D. Stone, J. D. Joannopoulos, and M. Soljačić, Bound states in the continuum, Nat. Rev. Mater. **1**, 16048 (2016).
[2] M. Kang, T. Liu, C. Chan, and M. Xiao, Applications of bound states in the continuum in photonics, Nat. Rev. Phys. **5**, 659 (2023).
[3] L. Huang, L. Xu, D. A. Powell, W. J. Padilla, and A. E. Miroshnichenko, Resonant leaky modes in all-dielectric metasystems: Fundamentals and applications, Phys. Rep. **1008**, 1 (2023).
[4] J. Wang, P. Li, X. Zhao, Z. Qian, X. Wang, F. Wang, X. Zhou, D. Han, C. Peng, L. Shi *et al.*, Optical bound states in the continuum in periodic structures: Mechanisms, effects, and applications, Photonics Insights **3**, R01 (2024).
[5] D. C. Marinica, A. G. Borisov, and S. V. Shabanov, Bound states in the continuum in photonics, Phys. Rev. Lett. **100**, 183902 (2008).
[6] C. W. Hsu, B. Zhen, J. Lee, S.-L. Chua, S. G. Johnson, J. D. Joannopoulos, and M. Soljačić, Observation of trapped light within the radiation continuum, Nature (London) **499**, 188 (2013).
[7] B. Zhen, C. W. Hsu, L. Lu, A. D. Stone, and M. Soljačić, Topological nature of optical bound states in the continuum, Phys. Rev. Lett. **113**, 257401 (2014).
[8] Y. Zhang, A. Chen, W. Liu, C. W. Hsu, B. Wang, F. Guan, X. Liu, L. Shi, L. Lu, and J. Zi, Observation of polarization vortices in momentum space, Phys. Rev. Lett. **120**, 186103 (2018).

[9] H. M. Doeleman, F. Monticone, W. den Hollander, A. Alù, and A. F. Koenderink, Experimental observation of a polarization vortex at an optical bound state in the continuum, Nat. Photonics **12**, 397 (2018).
[10] A. Tittl, A. Leitis, M. Liu, F. Yesilkoy, D.-Y. Choi, D. N. Neshev, Y. S. Kivshar, and H. Altug, Imaging-based molecular barcoding with pixelated dielectric metasurfaces, Science **360**, 1105 (2018).
[11] F. Yesilkoy, E. R. Arvelo, Y. Jahani, M. Liu, A. Tittl, V. Cevher, Y. Kivshar, and H. Altug, Ultrasensitive hyperspectral imaging and biodetection enabled by dielectric metasurfaces, Nat. Photonics **13**, 390 (2019).
[12] A. Kodigala, T. Lepetit, Q. Gu, B. Bahari, Y. Fainman, and B. Kanté, Lasing action from photonic bound states in continuum, Nature (London) **541**, 196 (2017).
[13] S. T. Ha, Y. H. Fu, N. K. Emani, Z. Pan, R. M. Bakker, R. Paniagua-Domínguez, and A. I. Kuznetsov, Directional lasing in resonant semiconductor nanoantenna arrays, Nat. Nanotechnol. **13**, 1042 (2018).
[14] C. Huang, C. Zhang, S. Xiao, Y. Wang, Y. Fan, Y. Liu, N. Zhang, G. Qu, H. Ji, J. Han *et al.*, Ultrafast control of vortex microlasers, Science **367**, 1018 (2020).
[15] M.-S. Hwang, H.-C. Lee, K.-H. Kim, K.-Y. Jeong, S.-H. Kwon, K. Koshelev, Y. Kivshar, and H.-G. Park, Ultralow-threshold laser using super-bound states in the continuum, Nat. Commun. **12**, 4135 (2021).
[16] Y.-G. Sang, J.-Y. Lu, Y.-H. Ouyang, H.-Y. Luan, J.-H. Wu, J.-Y. Li, and R.-M. Ma, Topological polarization singular lasing with highly efficient radiation channel, Nat. Commun. **13**, 6485 (2022).
[17] V. Ardizzone, F. Riminucci, S. Zanotti, A. Gianfrate, M. Efthymiou-Tsironi, D. Suàrez-Forero, F. Todisco, M. De Giorgi, D. Trypogeorgos, G. Gigli *et al.*, Polariton Bose–Einstein condensate from a bound state in the continuum, Nature (London) **605**, 447 (2022).
[18] A. Gianfrate, H. Sigurðsson, V. Ardizzone, H. C. Nguyen, F. Riminucci, M. Efthymiou-Tsironi, K. W. Baldwin, L. N. Pfeiffer, D. Trypogeorgos, M. De Giorgi *et al.*, Reconfigurable quantum fluid molecules of bound states in the continuum, Nat. Phys. **20**, 61 (2024).
[19] E. Maggiolini, L. Polimeno, F. Todisco, A. Di Renzo, B. Han, M. De Giorgi, V. Ardizzone, C. Schneider, R. Mastria, A. Cannavale *et al.*, Strongly enhanced light–matter coupling of monolayer WS2 from a bound state in the continuum, Nat. Mater. **22**, 964 (2023).
[20] T. Weber, L. Kühner, L. Sortino, A. Ben Mhenni, N. P. Wilson, J. Kühne, J. J. Finley, S. A. Maier, and A. Tittl, Intrinsic strong light-matter coupling with self-hybridized bound states in the continuum in van der Waals metasurfaces, Nat. Mater. **22**, 970 (2023).
[21] M. Cotrufo, A. Cordaro, D. L. Sounas, A. Polman, and A. Alù, Passive bias-free non-reciprocal metasurfaces based on thermally nonlinear quasi-bound states in the continuum, Nat. Photonics **18**, 81 (2024).
[22] B. Wang, W. Liu, M. Zhao, J. Wang, Y. Zhang, A. Chen, F. Guan, X. Liu, L. Shi, and J. Zi, Generating optical vortex beams by momentum-space polarization vortices centred at bound states in the continuum, Nat. Photonics **14**, 623 (2020).
[23] J. Wang, L. Shi, and J. Zi, Spin Hall effect of light via momentum-space topological vortices around bound states in the continuum, Phys. Rev. Lett. **129**, 236101 (2022).
[24] L. Allen, M. Padgett, and M. Babiker, IV The orbital angular momentum of light, in *Progress in Optics* (Elsevier, New York, 1999), Vol. 39, pp. 291–372.
[25] D. L. Andrews and M. Babiker, *The Angular Momentum of Light* (Cambridge University Press, Cambridge, England, 2012).
[26] Y. Shen, X. Wang, Z. Xie, C. Min, X. Fu, Q. Liu, M. Gong, and X. Yuan, Optical vortices 30 years on: OAM manipulation from topological charge to multiple singularities, Light **8**, 90 (2019).
[27] K. Y. Bliokh, F. J. Rodríguez-Fortuño, F. Nori, and A. V. Zayats, Spin–orbit interactions of light, Nat. Photonics **9**, 796 (2015).
[28] D. Song, V. Paltoglou, S. Liu, Y. Zhu, D. Gallardo, L. Tang, J. Xu, M. Ablowitz, N. K. Efremidis, and Z. Chen, Unveiling pseudospin and angular momentum in photonic graphene, Nat. Commun. **6**, 6272 (2015).
[29] X. Ling, X. Zhou, K. Huang, Y. Liu, C.-W. Qiu, H. Luo, and S. Wen, Recent advances in the spin Hall effect of light, Rep. Prog. Phys. **80**, 066401 (2017).
[30] J. Chen, C. Wan, and Q. Zhan, Vectorial optical fields: Recent advances and future prospects, Sci. Bull. **63**, 54 (2018).
[31] See Supplemental Material at http://link.aps.org/supplemental/10.1103/PhysRevLett.134.133802, which includes Refs. [4,7,8,22,32–37], for simulation methods, symmetry analysis based on group theory, details on sample fabrication, details on the optical measurement system, numerical results of the self-interference patterns for two types of BIC lasing, detailed experimental demonstrations of two types of topological BIC lasing, details on polarization-resolved lasing images, discussions on the emission efficiency, purity analysis for the OAM modes in BIC lasing, and measured self-interference patterns with different applied polarizations of the pump light.
[32] Z. Zhang, X. Qiao, B. Midya, K. Liu, J. Sun, T. Wu, W. Liu, R. Agarwal, J. M. Jornet, S. Longhi *et al.*, Tunable topological charge vortex microlaser, Science **368**, 760 (2020).
[33] N. Carlon Zambon, P. St-Jean, M. Milićević, A. Lemaître, A. Harouri, L. Le Gratiet, O. Bleu, D. Solnyshkov, G. Malpuech, I. Sagnes *et al.*, Optically controlling the emission chirality of microlasers, Nat. Photonics **13**, 283 (2019).
[34] Z. Che, Y. Zhang, W. Liu, M. Zhao, J. Wang, W. Zhang, F. Guan, X. Liu, W. Liu, L. Shi *et al.*, Polarization singularities of photonic quasicrystals in momentum space, Phys. Rev. Lett. **127**, 043901 (2021).
[35] K. Arjas, J. M. Taskinen, R. Heilmann, G. Salerno, and P. Törmä, High topological charge lasing in quasicrystals, Nat. Commun. **15**, 9544 (2024).
[36] Y. Zhang, M. Zhao, J. Wang, W. Liu, B. Wang, S. Hu, G. Lu, A. Chen, J. Cui, W. Zhang *et al.*, Momentum-space imaging spectroscopy for the study of nanophotonic materials, Sci. Bull. **66**, 824 (2021).
[37] B. Sephton, Y.-W. Huang, A. Ambrosio, C.-W. Qiu, A. Vallés, T. Omatsu, F. Capasso, and A. Forbes, Purity and

efficiency of hybrid orbital angular momentum-generating metasurfaces, J. Nanophoton. **14**, 016005 (2020).
[38] Z.-Q. Yang, Z.-K. Shao, H.-Z. Chen, X.-R. Mao, and R.-M. Ma, Spin-momentum-locked edge mode for topological vortex lasing, Phys. Rev. Lett. **125**, 013903 (2020).
[39] H. Qin, Z. Su, M. Liu, Y. Zeng, M.-C. Tang, M. Li, Y. Shi, W. Huang, C.-W. Qiu, and Q. Song, Arbitrarily polarized bound states in the continuum with twisted photonic crystal slabs, Light **12**, 66 (2023).
[40] X. Zhao, J. Wang, W. Liu, Z. Che, X. Wang, C. T. Chan, L. Shi, and J. Zi, Spin-orbit-locking chiral bound states in the continuum, Phys. Rev. Lett. **133**, 036201 (2024).
[41] J. Wang, M. Zhao, W. Liu, F. Guan, X. Liu, L. Shi, C. T. Chan, and J. Zi, Shifting beams at normal incidence via controlling momentum-space geometric phases, Nat. Commun. **12**, 6046 (2021).
[42] Y. Yu, A. Sakanas, A. R. Zali, E. Semenova, K. Yvind, and J. Mørk, Ultra-coherent fano laser based on a bound state in the continuum, Nat. Photonics **15**, 758 (2021).
[43] Y. Ren, P. Li, Z. Liu, Z. Chen, Y.-L. Chen, C. Peng, and J. Liu, Low-threshold nanolasers based on miniaturized bound states in the continuum, Sci. Adv. **8**, eade8817 (2022).
[44] M. Wu, S. T. Ha, S. Shendre, E. G. Durmusoglu, W.-K. Koh, D. R. Abujetas, J. A. Sánchez-Gil, R. Paniagua-Domínguez, H. V. Demir, and A. I. Kuznetsov, Room-temperature lasing in colloidal nanoplatelets via mie-resonant bound states in the continuum, Nano Lett. **20**, 6005 (2020).
[45] S. Mohamed, J. Wang, H. Rekola, J. Heikkinen, B. Asamoah, L. Shi, and T. K. Hakala, Controlling topology and polarization state of lasing photonic bound states in continuum, Laser Photonics Rev. **16**, 2100574 (2022).
[46] A. Forbes, L. Mkhumbuza, and L. Feng, Orbital angular momentum lasers, Nat. Rev. Phys. **6**, 352 (2024).
[47] D. Naidoo, F. S. Roux, A. Dudley, I. Litvin, B. Piccirillo, L. Marrucci, and A. Forbes, Controlled generation of higher-order poincaré sphere beams from a laser, Nat. Photonics **10**, 327 (2016).
[48] H. Sroor, Y.-W. Huang, B. Sephton, D. Naidoo, A. Vallés, V. Ginis, C.-W. Qiu, A. Ambrosio, F. Capasso, and A. Forbes, High-purity orbital angular momentum states from a visible metasurface laser, Nat. Photonics **14**, 498 (2020).
[49] M. Piccardo, M. de Oliveira, A. Toma, V. Aglieri, A. Forbes, and A. Ambrosio, Vortex laser arrays with topological charge control and self-healing of defects, Nat. Photonics **16**, 359 (2022).
[50] Z. Zhang, H. Zhao, S. Wu, T. Wu, X. Qiao, Z. Gao, R. Agarwal, S. Longhi, N. M. Litchinitser, L. Ge *et al.*, Spin–orbit microlaser emitting in a four-dimensional Hilbert space, Nature (London) **612**, 246 (2022).